PHYSICAL REVIEW RESEARCH **2**, 013296 (2020)

Rashba splitting of the Tamm surface state on Re(0001) observed by spin-resolved photoemission and scanning tunneling spectroscopy

H. J. Elmers,[1] J. Regel,[1] T. Mashoff,[1] J. Braun,[2] S. Babenkov,[1] S. Chernov,[1] O. Fedchenko,[1] K. Medjanik,[1] D. Vasilyev,[1]
J. Minar,[3] H. Ebert,[2] and G. Schönhense[1]
[1]*Institut für Physik, Johannes Gutenberg-Universität, Staudingerweg 7, D-55099 Mainz, Germany*
[2]*Ludwig Maximilians-Universität, München, Germany*
[3]*NTC, University of West Bohemia, Plzen, Czech Republic*

(Received 6 December 2019; accepted 19 February 2020; published 11 March 2020)

Using spin-resolved time-of-flight momentum microscopy, the Rashba splitting of the Tamm surface state is investigated. This state resides at the Fermi level in a projected bulk band gap of the close-packed (0001) surface of hcp Re. The Rashba splitting amounts to 0.4 Å^{-1}. The state with smaller parallel momentum is fully separated from bulk states, whereas the Rashba branch with larger momentum hybridizes with bulk states, which leads to a suppression of spin-momentum locking. We find a good agreement of the experimental results with one step photoemission calculations that are based on *ab initio* theory within the local density approximation. The spin polarization of the inner Rashba state is not complete, which manifests in the occurrence of quantum interference patterns as observed by scanning tunneling microscopy. A one-to-one agreement of scanning tunneling spectroscopy and photoemission results is observed, suggesting that the quantum interference pattern originates from the inner Rashba state.

DOI: 10.1103/PhysRevResearch.2.013296

I. INTRODUCTION

Electronic states emerging at the surface of high-Z materials have attracted much scientific interest, because the strong spin-orbit coupling in combination with the broken inversion symmetry and a strong effective electric field at the surface results in a strong spin-momentum locking [1–5]. These spin-momentum locked surface states are of interest in physics and materials technology, because their high mobility and topological protection promises novel applications in electronics and data processing [6]. As an example, the spin polarization of these states is currently discussed as an origin of an improved intrinsic conversion of light to electricity in perovskites [7,8].

Interestingly, the topological properties are not restricted to complex materials. A strong spin-momentum locking of surface states also appears in elemental metals [9–11], such as Au(111) and W(110). The projected band structure of Au(111) shows a hybridization gap near the Γ point hosting a surface state with orbital sp character and the Rashba-like spin-orbit interaction causes a spin splitting of this surface state [3,4,12,13] with topological character [14]. The (110) surface of tungsten has a spin-orbit induced local band gap for bulk states projected onto the surface, which is 200 meV wide and located at 1.25 eV below the Fermi energy [10]. A Dirac-like surface state with linear dispersion and Rashba-type spin signature resides within this gap. Further experimental [15–21] as well as theoretical work [10,11,18,22,23] revealed the orbital d character of surface states on W(110), which is in contrast to the common orbital sp character of surface states (Shockley-type surface states) of topological insulators. In this case the surface state has been identified as a surface resonance that extends into the bulk.

Therefore, the question arises whether fully surface-localized d-like surface states, which are confined between the surface potential barrier and a totally reflecting periodic potential, can reveal a significant spin-momentum locking. These Tamm-type surface states are located in a nonhybridization gap of the projected bulk band structure [24,25]. Their existence requires that the surface perturbation of the one-electron potential is sufficiently strong [26]. In early work, Tamm surface states were observed experimentally at the top of the bulk d-bands of Cu(100), Cu(111) [24,26–28], Ag(100) [27,29–31], Au(100) and Au(111) [24] by spin-integrated spectroscopy.

For the present study, we focus on the Re(0001) surface, for which a surface related state near the $\overline{\Gamma}$ point with d character and a Rashba spin-splitting has recently been predicted by density functional theory [32]. In this theoretical study this state appeared rather as a surface resonance because no gap in the projected bulk band structure exists. In contrast, differential conductance measurements on the Re(0001) surface revealed the presence of standing waves that have been attributed to a surface state [33], indicating their prominent surface localization. The Re(0001) surface offers the interesting property of causing nontrivial magnetization structures in adsorbed ultrathin ferromagnetic films [34]. A

---

recent study reports on the atomic-scale interface engineering of Majorana edge modes at the Fe/Re(0001)-O(2x1) interface [35]. Further recent studies comprise the growth of graphene [36], hBN [37], and Pd on Re(0001) [38]. These interesting properties ask for a comprehensive spin-resolved study of the Re(0001) bulk and surface states.

II. EXPERIMENTAL METHODS

All experiments were performed in ultra-high vacuum. The base pressure was in the low 10^{-10} mbar regime. For the preparation of clean Re(0001) surfaces we followed the recipe given in Ref. [33]. Our cleaning procedure consists of cycles of annealing at $T = 1400$ K with partial oxygen pressure of 3×10^{-8} mbar and high-temperature flashes at $T = 1800$–1850 K to desorb oxygen. After the preparation, the sample is transferred to the scanning tunneling microscopy (STM) and photoemission sample stages, respectively.

STM measurements were performed at 5 K using chemically etched tungsten tips, which were flashed at 2200 K [39]. Differential conductivity maps are recorded using a modulation frequency of 300 Hz and a lock-in amplifier.

We used time-of-flight (ToF) momentum microscopy [40,41] for photoemission spectroscopy in a separate setup. The momentum microscope images the transversal momentum component of the photoemitted electrons on a spatially resolving detector, which is combined with ToF detection for parallel recording of electrons with different kinetic energies [42]. The measurement results in the intensity as a function of binding energy and parallel momentum, $I(E_B, k_x, k_y)$. The sample is mounted on a He-cooled high-precision hexapod manipulator providing a minimum temperature of 29 K (measured by a silicon diode attached to the sample holder) and six degrees of freedom for sample alignment. The instrument comprises two ToF branches (see Fig. 1). Spin-integral measurements are performed with the straight branch, whereas for spin-resolved experiments a retractable spin-filter crystal reflects the electrons into the second branch under 45°.

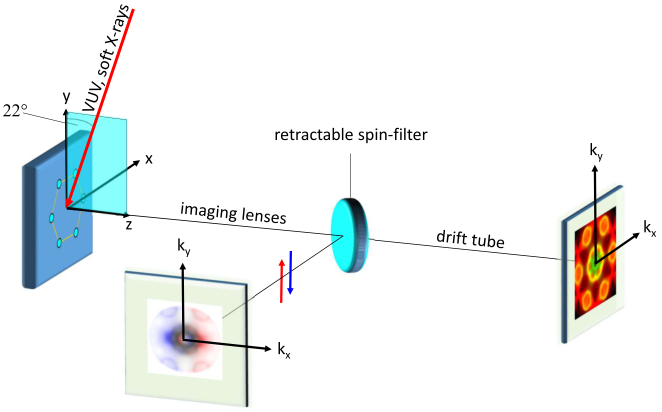

FIG. 1. Sketch of the experimental set-up for time-of-flight momentum microscopy. The hexagon on the sample surface indicates the unit cell of Re(0001) in real space. The images on the screens in the straight and spin-filter branch represent constant-energy maps of intensity and spin polarization, respectively. The red/blue arrows denote the quantization axis for the spin-resolved measurements. The incident light is *p*-polarized in the vacuum ultraviolet regime, whereas it is circular-polarized in the soft x-ray regime.

Spin-resolved images are obtained by inserting the Ir(001) spin-filter crystal covered with a pseudomorphic Au monolayer into the electron optical path of the microscope between column and the spin-resolved ToF branch. Spin contrast appears due to the spin dependent reflectivity of low-energy electrons at the scattering target caused by spin-orbit interaction at the nonmagnetic surface. For the evaluation of the spin polarization we followed the recipe described in Ref. [13]. Two datasets at two different scattering energies of 10.75 eV and 12.5 eV are acquired. The spin quantization axis is perpendicular to the scattering plane, i.e., along the $\overline{\Gamma}$-$\overline{K}$ direction, denoted as the y direction in our coordinate system. For the calculation of the spin polarization, reflected intensities for two scattering energies $I_{\mathrm{surf},i}$ $(i = h, l)$ with opposite sign of the Sherman function, S_i, have been measured.

The spin polarization at each image point then is determined by [43]

$$P_o = \frac{1 - \rho\psi}{\rho\psi S_l - S_h}, \qquad (1)$$

where $\psi = I_h/I_l$ is the ratio of measured intensities at each image point and $\rho = R_l/R_h$ denotes the ratio of the energy-dependent spin-integrated reflectivity R_h and R_l at both scattering energies. The energy dependence of S_i was neglected as we analyzed only a narrow energy interval of less than 1 eV. We have applied a symmetrization along k_y and antisymmetrization along k_x, $P(E_B, k_x, k_y) = [P_o(E_B, k_x, k_y) + P_o(E_B, k_x, -k_y) - P_o(E_B, -k_x, k_y) - P_o(E_B, -k_x, -k_y)]/4$. Note that the threefold symmetry of the Re(0001) surface breaking the x-z mirror symmetry is restored by the occurrence of terraces separated by monoatomic steps. Because of the time-reversal symmetry of the Rashba state, one obtains $I(k, \uparrow) = -I(-k, \downarrow)$, which justifies the applied symmetrizations.

The combination of the two values of the Sherman function for the low- and high-energy working points leads to an effective asymmetry function of $S_{\mathrm{eff}} = 0.7 \pm 0.1$. The error bar represents the uncertainty in the determination of the spin asymmetries and is partly of statistical and partly systematic nature.

The photoemission time-of-flight experiment has been performed exploiting the time structure of the synchrotron radiation at BESSY II (Helmholtz-Zentrum Berlin, Germany) at beamline U125/2-10m Normal Incidence Monochromator (NIM) during single-bunch operation (pulse duration 50 ps, repetition rate 1.25 MHz). The monochromator provides photons in the energy range 4 to 35 eV with an energy resolution of <10 meV. The angle of incidence was 68 degrees with respect to the surface normal, the plane of incidence was parallel to the $\overline{\Gamma}$-$\overline{K}$ direction (y axis). The photon beam was p-polarized with the electric field vector E in the plane of incidence. The overall energy and $k_{||}$ resolution for the present experiment were 86 meV and 0.03 Å^{-1}. Similar experiments with soft x-ray excitation have been performed at PETRA III (Desy, Hamburg) at beamline P04.

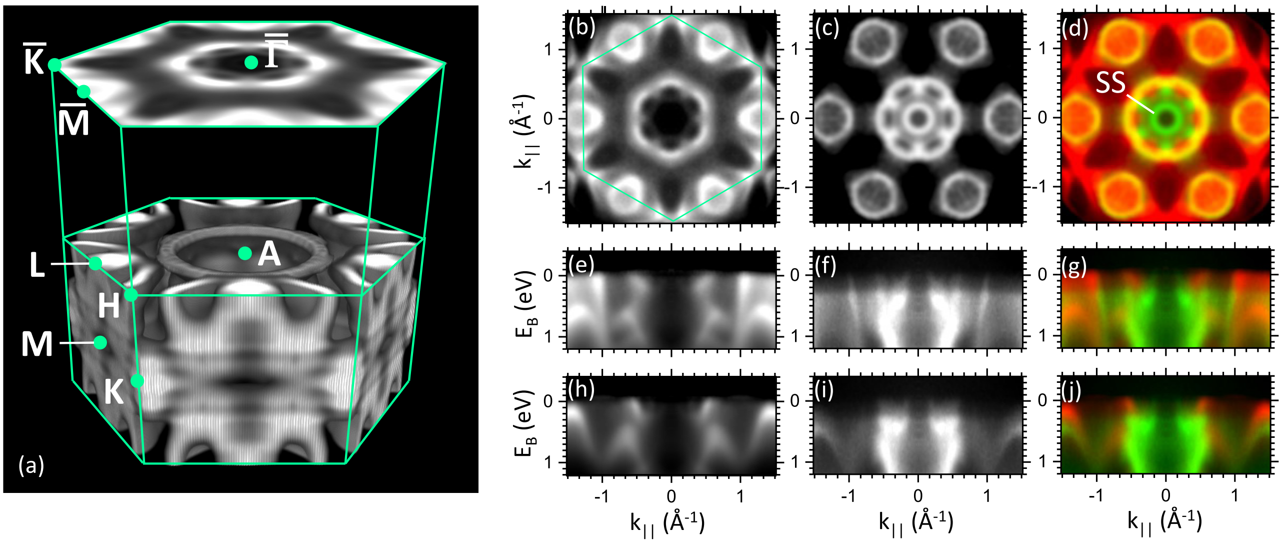

FIG. 2. (a) Bottom: three-dimensional representation of the measured spectral density of states of Re at the Fermi level $\rho(E_B = 0, k_x, k_y, k_z)$ (Fermi surface) with indicated Brillouin zone and high-symmetry points extracted from soft x-ray photoemission. (Top) Projected spectral density $\rho_{0001}(E_B = 0, k_x, k_y)$ for the Re(0001) surface resulting from an integration along the surface normal. (b) Constant-energy map of the projected spectral density of bulk states $\rho_{0001}(E_B = 0, k_x, k_y)$ from soft x-ray excitation. (c) Constant-energy map $\rho_{\mathrm{surf}}(E_B = 0, k_x, k_y)$ from excitation at a photon energy of 18.5 eV, revealing surface related states. (d) Overlay of surface (green) and projected bulk (red) states indicating pure surface states in green and surface resonances in yellow using adapted color scales. [(e)–(g)] Corresponding dispersion along $\overline{\Gamma}$-$\overline{M}$ and [(h)–(j)] along $\overline{\Gamma}$-$\overline{K}$, respectively.

III. THEORETICAL AND COMPUTATIONAL DETAILS

Calculations based on the fully relativistic one-step model of photoemission [44,45] in its spin-density matrix formulation [22,46] provides theoretical spectra. This approach allows describing properly the complete spin polarization vector in particular for the Rashba-type spin-momentum locked systems. The self-consistent electronic structure calculations were performed within the ab-initio framework of spin-density functional theory where the Vosko, Wilk, and Nusair parametrization for the exchange and correlation potential was used [47]. The corresponding electronic structure of the Re(0001) surface was calculated in a fully relativistic way using the multiple-scattering or KKR formalism in its tight-binding mode [48–50].

For all photoemission calculations, in addition, we account for the surface itself by use of a Rundgren-Malmström-type surface potential [51]. This allows for the correct description of the energetics and dispersion of all surface-related features, especially for the d-like surface resonance which is located in energy in the vicinity of the Fermi level. Furthermore, the relative intensities of surface states and resonances are quantitatively accounted for by calculating the corresponding matrix elements in the surface region. This procedure is described in detail, for example, in Ref. [52]. The energy-dependent retarded KKR Green function, which represents the initial state has been calculated for a complex energy, with an constant imaginary part $V_i(E) = 0.04$ eV, to account for hole life-time due to inelastic scattering events. Also in the final-state calculation many-body effects have been included phenomenologically to account for the inelastic mean free path (IMFP) of the high-energy photoelectron. In detail, a constant imaginary value of $V_i = 1.5$ eV was used. The spectroscopic calculations were performed with linear p-polarized light where a fixed polar angle of the incoming photon beam of $\theta = 68^o$ with respect to the surface normal was chosen, as in the experiment.

IV. RESULTS

First, we discuss the Re bulk states deduced from soft x-ray excitation (650–720) eV, where the higher kinetic energy of excited electrons results in an increased IMFP of the photoemitted electrons and consequently reduced spectral weight of surface states.

The momentum coordinate k_z results from scanning the photon energy, exploiting the concept of direct transitions as described in Refs. [42,53]. The constant-energy cuts for $E = E_F$ measured for 19 different photon energies in the range of (500–700) eV have been concatenated along k_z to form the three-dimensional Fermi surface. The variation of the photoemission intensity due to the dipole transition matrix elements, i.e., linear and circular dichroism, is accounted for by exploiting the sixfold symmetry in reciprocal space and averaging the illumination with circular left and right polarization. The data shown in Figs. 2 and 3 thus result from a sixfold symmetrization in momentum space of the measured intensity patterns. Consequently, the measured photoemission intensity $I(E_B, k_x, k_y, k_z)$ approximates the spectral density of states $\rho(E_B, k_x, k_y, k_z)$. Note that $I(E_B, k_x, k_y, k_z)$ does not exactly represent the spectral density because of different cross sections for different orbital character of the initial states. Surfaces of constant energy in three-dimensional k-space result from cuts of the four-dimensional array $\rho(E_B, k_x, k_y, k_z)$. The cut for $E_B = 0$ then represents the Fermi surface.

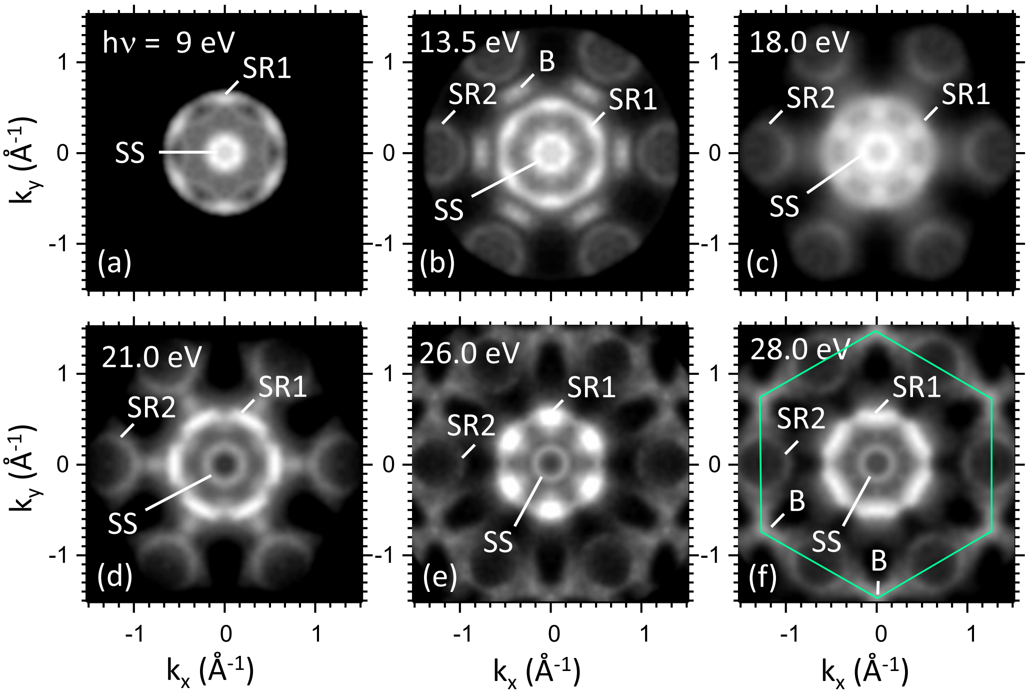

FIG. 3. Measured constant-energy maps $\rho_{\mathrm{surf}}(E_B = 0, k_x, k_y)$ for excitation with different photon energies as indicated in (a)–(f). The photon energy $h\nu = 18.5$ eV corresponds to $k_z = 2G_{0001}$ for normal emission, i.e., at Γ, in the free electron model. Features varying with photon energy indicate surface resonances (SR) or bulk states (B). The intensity of the surface state (SS) monotonously decreases with increasing photon energy indicating the pronounced localized character of the features emitted close to the surface normal.

Figure 2 shows the corresponding Fermi surface of Re. It comprises a prominent cylindrical sheet around the *c* axis and oblate ellipsoidal sheets centered at the *L* and *K* points.

By integrating ρ along k_z over the full Brillouin zone, i.e., parallel to the (0001) surface normal, one obtains the projected Fermi surface, $\rho_{0001}(E_B = 0, k_x, k_y)$, shown in a perspective view in Fig. 2(a) on top of the Brillouin zone and in planar view in Fig. 2(b). The center of the surface Brillouin zone is free of any projected bulk states, indicating the presence of a projected gap in the bulk band structure.

A similar projection performed with E_B as a parameter reveals the projected bulk band structure $\rho_{0001}(E_B, k_x, k_y)$ [Fig. 2(b)]. Cuts through $\rho_{0001}(E_B, k_x, k_y)$ along the in-plane high symmetry directions reveal the energy dispersion of the local gaps as shown in Figs. 2(e) and 2(h).

Excitation at photon energies in the vacuum ultraviolet range predominantly excites surface-related states of Re because of the limited IMFP of the photoemitted electrons. Fig. 2(c) shows the constant-energy map at the Fermi surface, $\rho_{\mathrm{surf}}(E_B = 0, k_x, k_y)$, obtained at a photon energy of 18.5 eV. We observe a sharp circle around the $\overline{\Gamma}$ point and a sextet of circles around the $\overline{M}$ points. Furthermore, two pronounced hexagonal structures with a flower-like shape, centered at the $\overline{\Gamma}$ point, dominate this Fermi surface map.

Figures 2(f) and 2(i) show the band dispersion along the high-symmetry directions $\overline{\Gamma}$-$\overline{M}$ and $\overline{\Gamma}$-$\overline{K}$. Most of the bands differ from the bands observed with soft x-ray excitation. In particular, the bands near the Fermi level close to $\overline{\Gamma}$ have a much stronger spectral weight compared to the soft x-ray measurement.

To determine the position of surface states relative to the projected bulk band gaps, we superimpose the projected density of bulk states [Figs. 2(b), 2(e) and 2(h)] with the surface sensitive photoemission result [Figs. 2(c), 2(f) and 2(i)], as depicted in Figs. 2(d), 2(g) and 2(j) [54].

For these overlaid images [Figs. 2(d), 2(g) and 2(j)], we apply a color code: red for the projected bulk states from the soft x-ray data and green for the spectral density deduced from the data at 18.5 eV excitation. The intensity of the projected bulk states and surface states have been adapted for better visibility. Note that the steplike increase of the (green) surface related spectral density at a binding energy of 0.3 eV may is not present in all measurements and may originate from adsorbates. Areas in the momentum cuts, where both measurements reveal a large spectral density, appear in the mixed color yellow. These yellow areas thus indicate surface resonances. We therefore tentatively attribute the $\overline{M}$ point circles and the outer $\overline{\Gamma}$ hexagon within the Fermi surface map [Fig. 2(e)] to surface resonances.

Correspondingly, the green color of the central ring in Fig. 2(d) indicates its pure surface state character. This state has hole character, i.e., negative group velocity, as deduced from the band dispersions shown in Figs. 2(g), 2(j).

To verify the surface or bulk character of electronic states, we varied the photon energy in a range from $h\nu = 7$–35 eV in steps of 0.5 eV. Figure 3 depicts selected constant-energy maps at the Fermi level. The inner ring structure SS, centered at $\overline{\Gamma}$, similarly appears for all photon energies with the same diameter, confirming its surface state character. Further data evaluation of the inner ring SS reveals a monotonously decreasing photoemission intensity with increasing photon

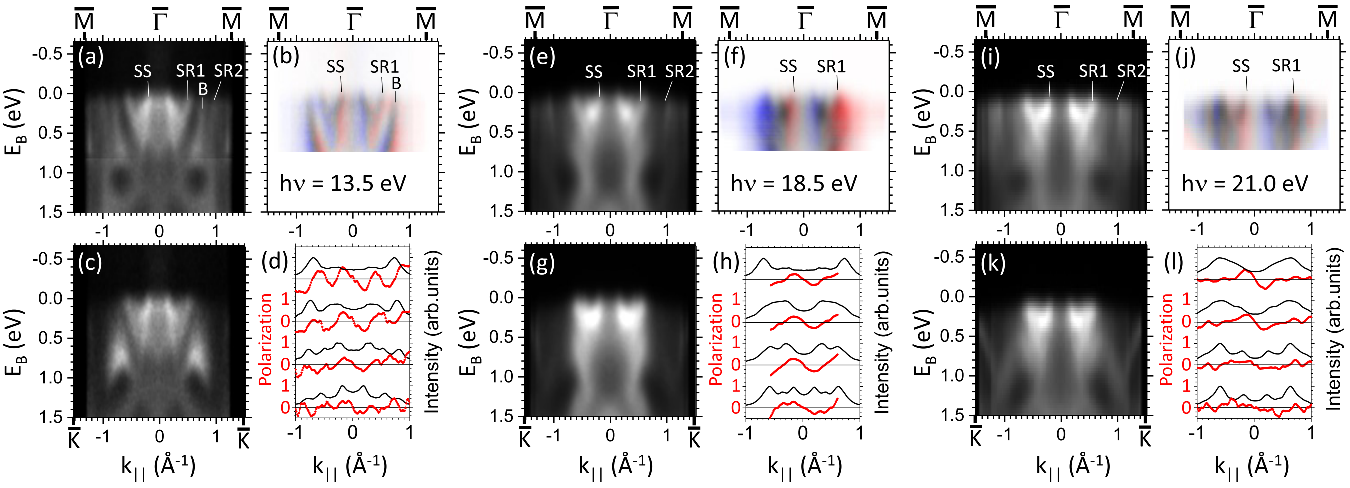

FIG. 4. Measured band dispersion and spin texture along the high symmetry directions $\overline{\Gamma}$-$\overline{M}$ (first row) $\overline{\Gamma}$-$\overline{K}$ (second row) for three photon energies as denoted. (a), (e), (i) and (c), (g), (k) show $E_B(k_x)$ and $E_B(k_y)$ sections of the spectral density $\rho_{\text{surf}}(E_B, k_x = 0, k_y)$ and $\rho_{\text{surf}}(E_B, k_x, k_y = 0)$, respectively. (b), (f), and (j) show the corresponding spin textures for the $\overline{\Gamma}$-$\overline{M}$ direction. The color code for spin polarization and intensity is given in Fig. 5. [(d), (h), and (l)] Profiles revealing the y component of the spin polarization P as a function of parallel momentum along $\overline{\Gamma}$-$\overline{M}$ for constant binding energies $E_B = 0$, 0.2, 0.4, and 0.6 eV (from bottom to top).

energy. This behavior indicates a state that is strongly localized at or even in front of the surface [55], because an extension into the bulk always leads in the reciprocal space to an oscillatory k_z and hence photon energy dependence. In contrast, the six $\overline{M}$ - rings SR show a low intensity at 26 eV and increasing intensity for 28 eV, revealing their surface resonance character with nonvanishing appearance probability deeper in the bulk. The intensity of the larger hexagonal structure SR1 also varies nonmonotonously with photon energy, also indicating a surface resonance. For all features named SS or SR, we do not observe any k_z dispersion. Despite of the limited mean free path of less than 3 Å [56], bulk states show up, too. For a photon energy of 13.5 eV a bulk state appears along the $\overline{\Gamma}$-$\overline{M}$ path. At 26–28 eV, a threefold starlike feature appears at the $\overline{K}$ point. Both features reveal a rapid k_z dispersion, indicating their bulk character. From the occurrence of bulk states, we estimate the k_z component of the photoelectron momentum. The photon energy of 18.5 eV corresponds to $k_z = 2G_{0001}$ ($G_{0001} = 1.4$ Å^{-1} for Re) at $\overline{\Gamma}$, in agreement with the free electron model $k_z = 0.512\sqrt{(h\nu + E_i)/\text{eV}}$ Å^{-1} with an inner potential of $E_i = 11.5$ eV, assuming an effective electron mass $m = m_e$.

We now turn to the results obtained in the spin branch of the microscope. To increase the statistical significance, we have symmetrized the intensity data shown in Figs. 4 and 5 with respect to k_x and k_y, $\rho_{\text{surf}}(E_B, k_x, k_y) = I_{\text{surf}}(E_B, k_x, k_y) + I_{\text{surf}}(E_B, -k_x, k_y) + I_{\text{surf}}(E_B, k_x, -k_y) + I_{\text{surf}}(E_B, -k_x, -k_y)$.

Fig. 4 shows the band dispersion along the indicated high-symmetry directions. Photoemission intensities and spin polarizations for the three photon energies 13.5, 18.5, and 21.0 eV are compared. The intensity sections for the three photon energies are shown in Figs. 4(a) and 4(c), 4(e) and 4(g), and 4(i) and 4(k) and the spin textures in (b), (f), and (j), respectively. Quantitative values for intensity and spin polarization are given in Figs. 4(d), 4(h) and 4(l). The surface state SS near the $\overline{\Gamma}$ point has the highest intensity. Its dispersion reveals a group velocity of $-(4.8 \pm 0.7)$ eVÅ independent on the parallel momentum direction. At $E_B = 0.2$ eV it starts to hybridize with the Re bulk state that is close to the Γ point. This becomes most obvious for $h\nu = 18.5$ eV. At this photon energy the final state sphere intersects the Γ point [see Figs. 4(e) and 4(f)]. In contrast, for the case of $h\nu = 13.5$ eV the isolated surface state can be observed up to a binding energy of 0.7 eV [see Figs. 4(a) and 4(b)].

The surface state (SS) shows an opposite spin polarization for positive and negative momentum with the spin direction to the right (blue for $k_x > 0$) with respect to the propagating direction of the electron. This spin orientation is expected for the inner Rashba state with smaller absolute momentum value. The surface resonance (SR1) next to the surface state has the opposite (red for $k_x > 0$) spin orientation. The $\overline{M}$ point surface resonance (SR2) has a weak spin polarization but possesses a predominant positive (red) polarization for $k_x > 0$, corresponding to a clockwise spin direction around the $\overline{M}$ point. For the 18.5 eV measurement, only spin polarization data for $|k_{\parallel}| < 0.7$ Å^{-1} could be evaluated.

For $h\nu = 13.5$ eV, we also observe the bulk state (B) as deduced from the pronounced k_z dispersion as already discussed for the spin-integrated results. The spin polarization of this bulk state vanishes at E_F within the error limits [Fig. 4(b)].

Figure 5 shows details of the intensity and spin polarization distributions in the constant-energy map representation. Note that the inner Rashba-type ring structure occurs independently on the photon energy. The outer Rashba ring is almost suppressed due to the hybridization with bulk states. For the case of 18.5 eV excitation, the coincidence of bulk and surface state intensity leads to a pronounced opposite spin polarization [Fig. 5(b)] of the inner (SS) and outer (SS') Rashba ring. For 13.5 eV excitation, both Rashba states become visible [Fig. 5(a)] at a binding energy of 400 meV. The maximum observed spin polarization of the Rashba split surface state amounts to $P = 0.7$.

Figure 6 depicts the *ab initio* calculated constant energy maps of the removal part of the spectral density, considering

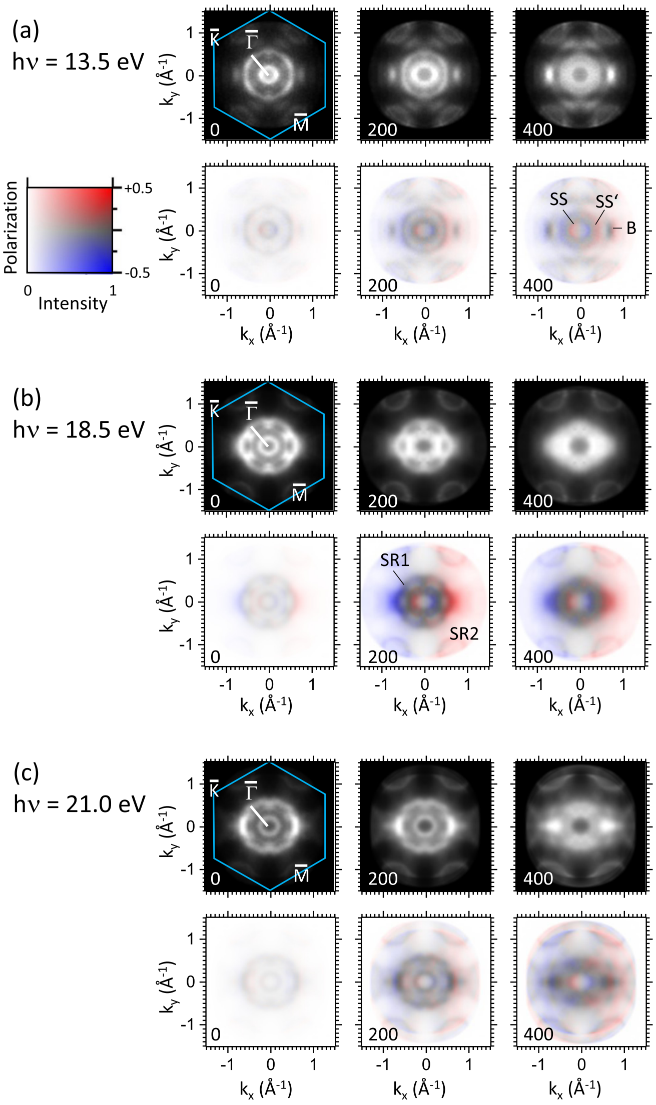

FIG. 5. (a) Top row: Constant-energy maps $\rho_{\mathrm{surf}}(E_B, k_x, k_y)$ measured for excitation with a photon energy of 13.5 eV. From left to right: $E_B = 0$, 200, 400 meV. Bottom row: constant-energy spin polarization maps $P_{\mathrm{surf}}(E_B, k_x, k_y)$. Color code for intensity and spin polarization indicated on the left. Corresponding data for a photon energy of 18.5 (b) and 21 eV (c).

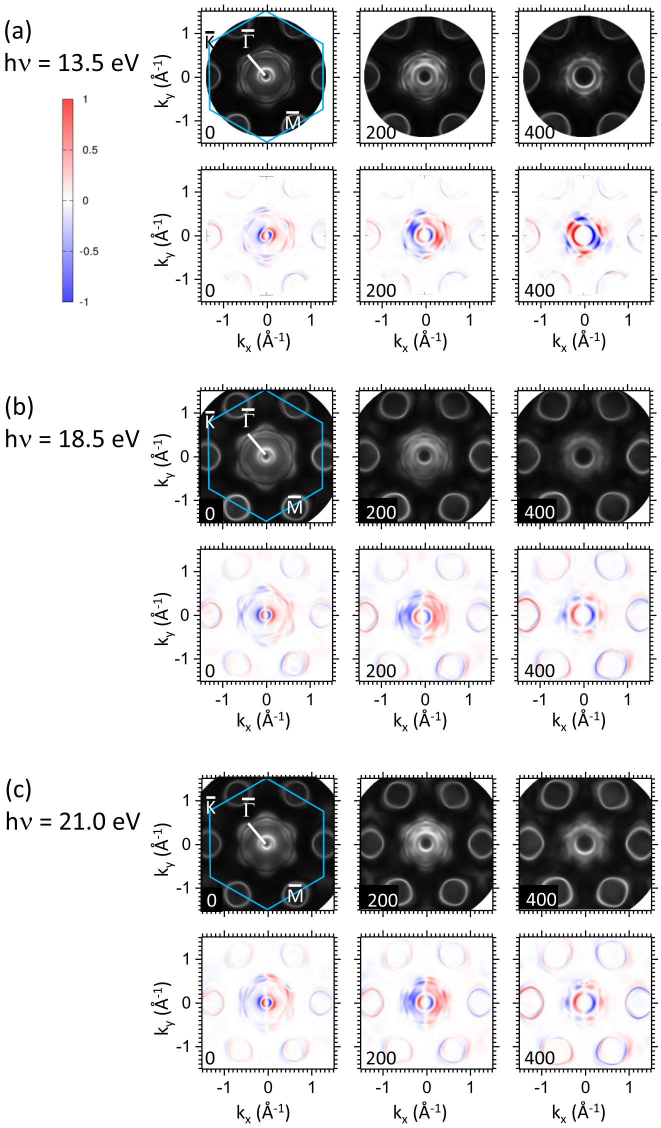

FIG. 6. (a) Top row: Calculated constant-energy maps using one-step photoemission calculations $I_{\mathrm{theo}}(E_B, k_x, k_y)$ for excitation with a photon energy of 13.5 eV. From left to right: $E_B = 0$, 200, and 400 meV. Bottom row: calculated constant-energy spin polarization maps $P_{y,\mathrm{theo}}(E_B, k_x, k_y)$. Corresponding theoretical data for a photon energy of 18.5 (b) and 21 eV (c).

a probability density in the first three surface layers. The one-step photoemission calculation considers the matrix element for the experimental geometry and photon energies. Constant-energy maps are calculated for three different photon energies corresponding experiment. The calculated spectral densities reveal the Rashba-split surface state in good agreement with the experimental result. While the inner Rashba state lies within the projected band gap close to the Fermi level, the outer Rashba state coincides with the projected bulk bands. Further bands with a high density probability occur at $k_\parallel \approx 0.5$ Å^{-1} and a band with almost circular shape is centered at the $\overline{M}$ points.

The spin-integrated intensities are in fair agreement with the experimental results (see Fig. 5). In the calculated spectral densities, the inner and outer Rashba bands are clearly separated and the outer Rashba branch appears broader than the inner branch, indicating its hybridization with bulk bands. Except for the relative intensities, the position of the surface state and surface resonances are independent of the photon energy. In contrast to the experimental results no clear bulk bands appear, which would be recognizable by their photon energy dependence. This might be explained by a slightly larger information depth in the experiment than parametrized for the calculation.

Figure 6 shows the calculated spin polarization component P_y along the k_y axis. The pair of split Rashba circles centered at the $\overline{\Gamma}$ point possess opposite spin polarization in good agreement with the experimental result. While the inner Rashba circle keeps its regular spin polarization texture with the constant spin direction always pointing perpendicular to

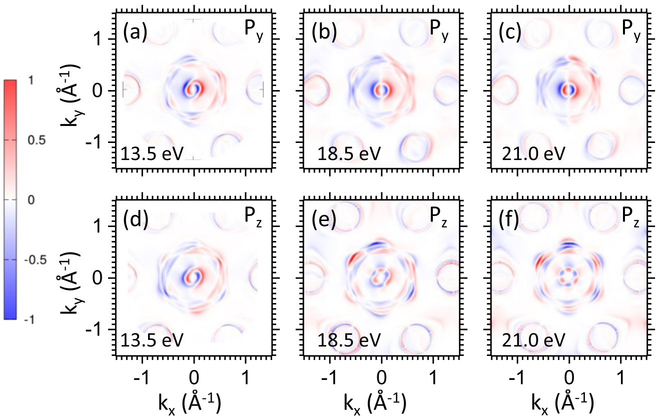

FIG. 7. [(a)–(c)] Calculated constant-energy maps of the spin polarization $P_{y,\mathrm{theo}}(E_F, k_x, k_y)$ at the Fermi energy using one-step photoemission calculations for excitation with photon energies of 13.5, 18.5, and 21 eV. (d)–(f) same for $P_{z,\mathrm{theo}}(E_F, k_x, k_y)$.

the parallel momentum vector, the outer Rashba circle shows a spin texture with increasing complexity for larger binding energies. This behavior is also attributed to the increasing hybridization of the outer Rashba branch with the Re bulk states. Interestingly, the antisymmetry $P(k_x) = -P(-k_x)$ is not perfectly fulfilled. This effect becomes most obvious for the photon energy of 13.5 eV. A calculation for the unoccupied part of the band structure reveals that the broken symmetry represents a final-state effect that vanishes for photon energies above 20 eV and below 10 eV, where no final states except for the free electron like states are present. The irregular spin texture is directly related to the absence of the mirror symmetry of the Re(0001) surface geometry with respect to the x-z plane.

Furthermore, calculations reveal nonvanishing values for the P_z spin polarization component. Figure 7 shows the comparison of the P_x and P_y component of the spin polarization as calculated by one-step photoemission theory. Similar to the case of the P_y component a final state effect leads to a modification of the P_z spin polarization of photoemitted electrons. For 13.5 eV, where the final state effect is strongest, the P_z and P_y polarization values appear similar to each other, highlighting this effect. For 21 eV, the final state effect becomes less prominent. Hence, the spin polarization predominantly reflects the initial state spin polarization. In addition to the Rashba-like in-plane spin texture, the threefold symmetry leads to a nonvanishing initial state P_z component with threefold symmetry.

Note that for a surface with monoatomic terraces, an averaging over these terraces restores the x-z mirror symmetry and as a consequence the symmetry relation $P(k_y) = P(-k_y)$ exploited for the analysis of the experimental data.

The *ab initio* result for the Bloch spectral function of the Re(0001) surface is shown in Fig. 8(a). Close to the $\overline{\Gamma}$ point one observes the Rashba split surface state with equal dispersion along $\overline{\Gamma}$-$\overline{K}$ and $\overline{\Gamma}$-$\overline{M}$. Figures 8(b) and 8(c) reveal the good agreement with the experimentally observed dispersion. The position of the experimental surface bands, indicated by the red dotted lines coincide almost perfectly with the inner Rashba band and also with the $\overline{M}$-point surface state. The outer Rashba state appears in the calculation with pronounced intensity, whereas it is weak in the experimental result. The spin polarization calculation clearly reflects the opposite sign of the spin polarization of the inner and outer Rashba state.

To visualize the surface state in real space, we performed scanning tunneling spectroscopy. The differential conductivity map shown in Fig. 9(a) reveals the quantum interference pattern resulting from back-scattering of the electron wave from step edges [33,57,58]. The figure shows two parallel monoatomic steps on the Re(0001) surface appearing as dark lines. In some areas the parallel steps form a quantum well, enhancing the amplitude of the interference pattern. Adsorbed gas molecules from the residual gas (presumably CO molecules) lead to additional circular shaped interference patterns (some denoted by arrows). The wavelength of the interference pattern increases with increasing tip-sample voltage, i.e., with decreasing binding energy. The power spectrum of the two-dimensional Fourier transformation [Fig. 9(b)] shows a circular feature revealing that the wavelength of the interference pattern is independent on the momentum direction. The tip-sample voltage of −50 meV addresses the unoccupied part of the surface state, 50 meV above E_F. The central line-shaped structure stems from the steps on the substrate surface. The circular feature refers to the inner Rashba state as observed by photoemission spectroscopy. The dispersion of the Rashba state has been elucidated by varying the tip-sample voltage. Figures 9(c)–9(f) show two examples of patterns recorded in the occupied part at 50 and 125 meV below E_F.

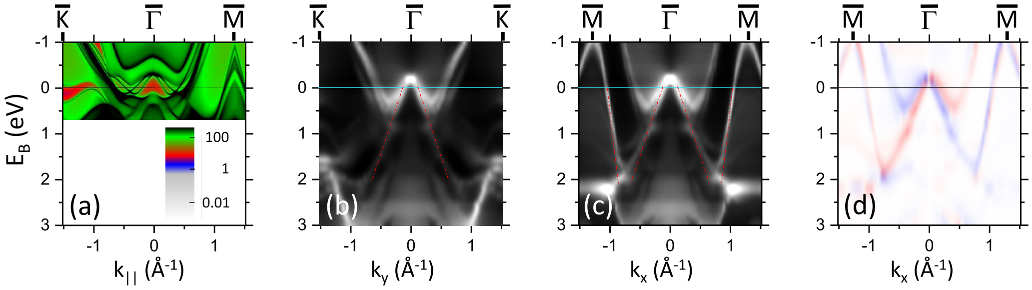

FIG. 8. (a) Bloch spectral function for Re(0001). Logarithmic intensity scale indicated by color code. (b) One step photoemission calculation for spin-integrated intensity, section along $\overline{\Gamma}$-$\overline{K}$. Red dotted line indicates experimentally observed surface states. (c) Same as (b) but along $\overline{\Gamma}$-$\overline{M}$, symmetrized to eliminate linear dichroism. (d) One step photoemission calculation of the spin polarization along $\overline{\Gamma}$-$\overline{M}$.

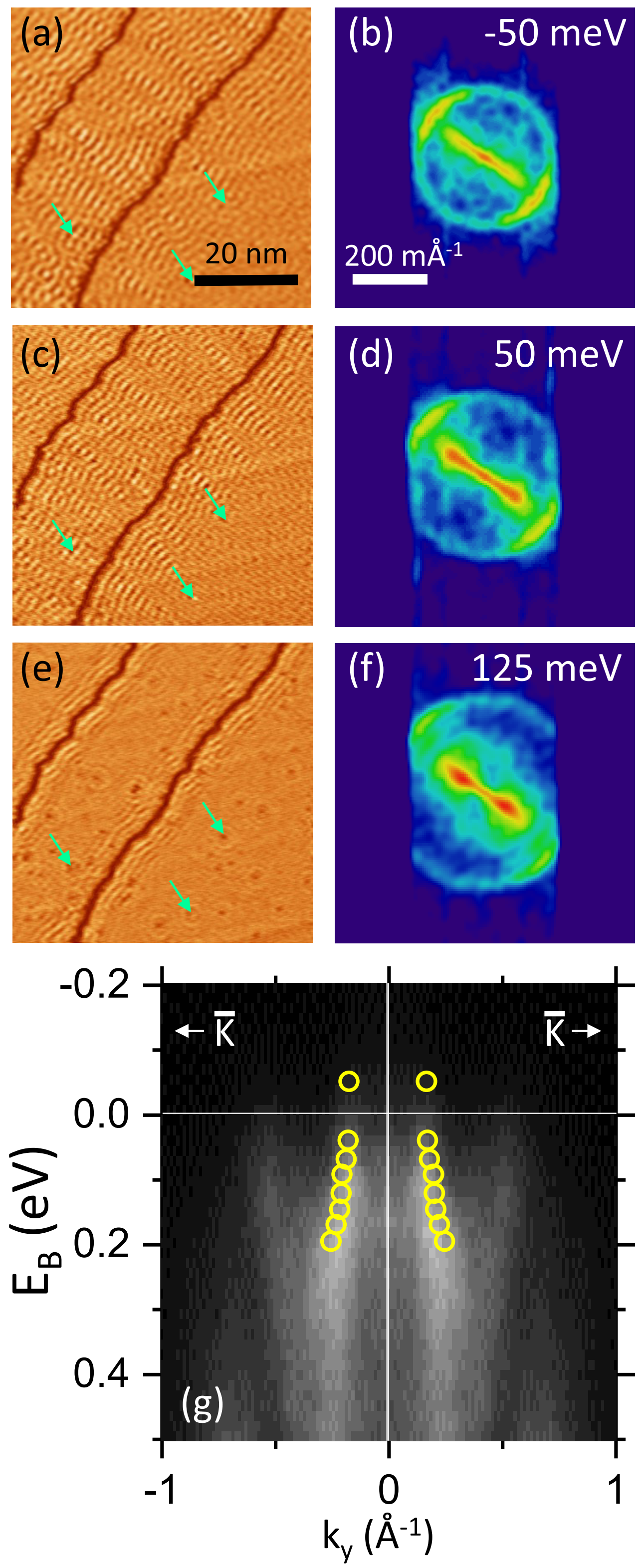

FIG. 9. (a) Differential conductivity map using scanning tunneling spectroscopy for tip-sample voltage of -50 mV. (b) Power spectrum of the Fourier transformation of (a) representing the momentum distribution of the quantum interference pattern. [(c) and (d)] Similar data for a tip-sample voltage of $+50$ mV and [(e) and (f)] $+125$ mV. (g) Overlay of photoemission intensity in the section along $\overline{\Gamma}$-$\bar{K}$ and results from differential conductivity maps. Yellow circles indicate half of the scattering vector.

Figure 9(g) compares the band dispersion as deduced from a series of eight differential conductivity maps at varying tip-sample voltage with the photoemission result. We observe a one-to-one agreement of scanning tunneling spectroscopy and photoemission results, confirming that the quantum interference pattern originates from the inner Rashba state. For binding energies above 0.2 eV and below -0.1 eV, the amplitude of the interference pattern becomes very weak preventing the determination of the wavelength. The decreasing amplitude might be a fingerprint of increasing hybridization with bulk states.

The origin of quantum interference patterns resulting from scattering between states with opposite spin is not obvious. Wiebe *et al.* [57] argued that the influence of spin polarization on scattering states could be too small to be observable. Wang *et al.* [59] calculated the spin-dependent joint density of states for scattered states in the case of Rashba splitting and topological states, resulting in the fact that a scattering vector connecting opposite spin states leads to a more rapid decay of the quasi particle interference, but not to a complete suppression. In this case of intra-band scattering the relevant scattering vector remains $q = 2k$ as in the case of spin-degenerate states. In contrast, El-Kareh *et al.* [60] argued that time-reversal symmetry prohibits a scattering from k to $-k$ between time-reversal partners and attribute the quasi particle interference to inter-band scattering, i.e. from the inner Rashba state to the outer Rashba state with the same spin. Such inter-band scattering would immediately explain the absence of the outer Rashba state in the Fourier transformed scanning tunneling spectroscopy images. In our case, the dispersion deduced from the quasi particle interference coincides with the dispersion observed by photoemission. The coincidence of photoemission and scanning tunneling spectroscopy results seems to favor the intra-band scattering model. In this case, the absence of the second Rashba branch may also be explained by a hybridization of the outer Rashba state with the bulk continuum, resulting in a loss of spectral weight in the vacuum [57].

V. CONCLUSION

In conclusion, we have determined the spin polarization of photoemitted electrons from the Re(0001) surface using spin-resolved time-of-flight momentum microscopy. In particular, we investigated the Rashba splitting of the Tamm surface state near the Γ point. We verified by angular-resolved photoemission that the surface state resides within a projected bulk band gap and shows a Rashba splitting of 0.4 Å^{-1}. The state with smaller parallel momentum (inner Rashba state) is fully separated from bulk states, whereas the Rashba branch with larger momentum hybridizes with bulk states, which leads to a suppression of spin-momentum locking. The presence of a single spin-momentum locked branch looks like the case of the Dirac-cone surface resonance at W(110) [61] that appears in a spin-orbit induced hybridization gap. However, in the present case the inner branch of the Rashba-split Tamm state is a true surface state with zero overlap with bulk bands. A good agreement of the experimental results with one-step photoemission calculations based on ab-initio theory within the local density approximation reveals the good understanding of the spin-momentum locking for Tamm surface states, appearing in a nonhybridization gap.

Differential conductivity maps obtained by scanning tunneling spectroscopy show quantum interference patterns. Two-dimensional Fourier transformations of these patterns agree perfectly with the constant energy photoelectron momentum distributions measured by photoemission and thus confirm that they result from the inner Rashba branch of the Rashba-split Tamm surface state. The apparently forbidden scattering path k to $-k$ has been discussed controversially in literature. Since this is beyond the scope of the present paper we do not review the various systems where quantum interference patterns have been observed and the tentative models discussed in Refs. [57,59,60]. The back-scattering of the surface states might allow for a versatile manipulation of the surface state by quantum confinement.

ACKNOWLEDGMENTS

Funding by BMBF (05K16UMB and 05K16WMA) and by the Deutsche Forschungsgemeinschaft (DFG, German Research Foundation) - TRR 173 – 268565370 is gratefully acknowledged. We thank the staffs of BESSY II (U125-2, 10mNIM) and PETRA III (beamline P 04) for excellent support at the beamline. J.M. would like to thank the CEDAMNF (CZ.02.1.01/0.0/0.0/15_003/0000358) co-funded by the ERDF as part of the Ministry of Education, Youth and Sports of Czech Republic.

---

[1] A. Tamai, W. Meevasana, P. D. C. King, C. W. Nicholson, A. de la Torre, E. Rozbicki, and F. Baumberger, Phys. Rev. B **87**, 075113 (2013).

[2] M. Hoesch, M. Muntwiler, V. N. Petrov, M. Hengsberger, L. Patthey, M. Shi, M. Falub, T. Greber, and J. Osterwalder, Phys. Rev. B **69**, 241401(R) (2004).

[3] F. Reinert, G. Nicolay, S. Schmidt, D. Ehm, and S. Hüfner, Phys. Rev. B **63**, 115415 (2001).

[4] S. LaShell, B. A. McDougall, and E. Jensen, Phys. Rev. Lett. **77**, 3419 (1996).

[5] E. I. Rashba, Sov. Phys. Solid State **2**, 1109 (1960).

[6] S. Wolf, D. Awschalom, R. Buhrman, J. Daughton, S. von Molnar, M. Roukes, A. Chtchelkanova, and D. Treger, Science **294**, 1488 (2001).

[7] Z.-G. Yu, J. Phys. Chem. Lett. **7**, 3078 (2016).

[8] F. Zheng, L. Z. Tan, S. Liu, and A. M. Rappe, Nano Lett. **15**, 7794 (2015).

[9] A. Varykhalov, D. Marchenko, M. R. Scholz, E. D. L. Rienks, T. K. Kim, G. Bihlmeyer, J. Sánchez-Barriga, and O. Rader, Phys. Rev. Lett. **108**, 066804 (2012).

[10] K. Miyamoto, A. Kimura, T. Okuda, K. Shimada, H. Iwasawa, H. Hayashi, H. Namatame, M. Taniguchi, and M. Donath, Phys. Rev. B **86**, 161411(R) (2012).

[11] K. Miyamoto, A. Kimura, K. Kuroda, T. Okuda, K. Shimada, H. Namatame, M. Taniguchi, and M. Donath, Phys. Rev. Lett. **108**, 066808 (2012).

[12] F. Reinert, J. Phys. Cond. Mat. **15**, S693 (2003).

[13] C. Tusche, A. Krasyuk, and J. Kirschner, Ultramic. **159**, 520 (2015).

[14] B. Yan, B. Stadtmueller, N. Haag, S. Jakobs, J. Seidel, D. Jungkenn, S. Mathias, M. Cinchetti, M. Aeschlimann, and C. Felser, Nat. Commun. **6**, 10167 (2015).

[15] A. Varykhalov, D. Marchenko, J. Sanchez-Barriga, E. Golias, O. Rader, and G. Bihlmayer, Phys. Rev. B **95**, 245421 (2017).

[16] D. Kutnyakhov, S. Chernov, K. Medjanik, R. Wallauer, C. Tusche, M. Ellguth, S. A. Nepijko, M. Krivenkov, J. Braun, S. Borek, J. Minar, H. Ebert, H. J. Elmers, and G. Schönhense, Sci. Rep. **6**, 29394 (2016).

[17] K. Honma, T. Sato, S. Souma, K. Sugawara, Y. Tanaka, and T. Takahashi, Phys. Rev. Lett. **115**, 266401 (2015).

[18] H. Mirhosseini, F. Giebels, H. Gollisch, J. Henk, and R. Feder, New J. Phys. **15**, 095017 (2013).

[19] H. Mirhosseini, M. Flieger, and J. Henk, New J. Phys. **15**, 033019 (2013).

[20] A. M. Shikin, A. Varykhalov, G. V. Prudnikova, D. Usachov, V. K. Adamchuk, Y. Yamada, J. D. Riley, and O. Rader, Phys. Rev. Lett. **100**, 057601 (2008).

[21] A. G. Rybkin, E. E. Krasovskii, D. Marchenko, E. V. Chulkov, A. Varykhalov, O. Rader, and A. M. Shikin, Phys. Rev. B **86**, 035117 (2012).

[22] J. Braun, K. Miyamoto, A. Kimura, T. Okuda, M. Donath, H. Ebert, and J. Minar, New J. Phys. **16**, 015005 (2014).

[23] K. Miyamoto, A. Kimura, T. Okuda, and M. Donath, J. Electron Spectrosc. Relat. Phenom. **201**, 53 (2015), special issue on electron spectroscopy for Rashba spin-orbit interaction.

[24] P. Heimann, J. Hermanson, H. Miosga, and H. Neddermeyer, Phys. Rev. Lett. **42**, 1782 (1979).

[25] A. Goldmann and R. Matzdorf, *Surface Science, Principles and Current Applications*, edited by R. J. MacDonald, E. C. Taglauer, and K. R. Wandelt (Springer, Berlin, 1996).

[26] P. Heimann, J. Hermanson, H. Miosga, and H. Neddermeyer, Phys. Rev. B **20**, 3059 (1979).

[27] S. D. Kevan, N. G. Stoffel, and N. V. Smith, Phys. Rev. B **32**, 4956 (1985).

[28] P. L. Wincott, N. B. Brookes, D. S.-L. Law, and G. Thornton, Phys. Rev. B **33**, 4373(R) (1986).

[29] H. Neddermeyer, J. Phys. F **12**, L241 (1982).

[30] A. Goldmann and E. Bartels, Surf. Sci. Letts. **122**, L629 (1982).

[31] T. Padmore, G. Thornton, and H. Padmore, Sol. Stat. Comm. **67**, 163 (1988).

[32] A. Urru and A. Dal Corso, Surf. Sci. **686**, 22 (2019).

[33] S. Ouazi, T. Pohlmann, A. Kubetzka, K. von Bergmann, and R. Wiesendanger, Surf. Sci. **630**, 280 (2014).

[34] A. Palacio-Morales, A. Kubetzka, K. von Bergmann, and R. Wiesendanger, Nano Lett. **16**, 6252 (2016).

[35] A. Palacio-Morales, E. Mascot, S. Cocklin, H. Kim, S. Rachel, D. K. Morr, and R. Wiesendanger, Sci. Adv. **5**, eaav6600 (2019).

[36] M. Papagno, P. Moras, P. M. Sheverdyaeva, J. Doppler, A. Garhofer, F. Mittendorfer, J. Redinger, and C. Carbone, Phys. Rev. B **88**, 235430 (2013).

[37] Y. Qi, Z. Zhang, B. Deng, X. Zhou, Q. Li, M. Hong, Y. Li, Z. Liu, and Y. Zhang, J. Am. Chem. Soc. **139**, 5849 (2017).

[38] H. A. Etman, Z. V. Zheleva, G. Held, and R. A. Bennett, J. Phys. Chem. C **115**, 4191 (2011).
[39] M. Bode, Rep. Prog. Phys. **66**, 523 (2003).
[40] G. Schönhense, K. Medjanik, S. Chernov, D. Kutnyakhov, O. Fedchenko, M. Ellguth, D. Vasilyev, A. Zaporozhchenko-Zymakova, D. Panzer, A. Oelsner, C. Tusche, B. Schonhense, J. Braun, J. Minar, H. Ebert, J. Viefhaus, W. Wurth, and H. J. Elmers, Ultramic. **183**, 19 (2017).
[41] G. Schönhense, K. Medjanik, and H.-J. Elmers, J. Electron Spectrosc. Relat. Phenom. **200**, 94 (2015).
[42] K. Medjanik, O. Fedchenko, S. Chernov, D. Kutnyakhov, M. Ellguth, A. Oelsner, B. Schonhense, T. R. F. Peixoto, P. Lutz, C. H. Min, F. Reinert, S. Daster, Y. Acremann, J. Viefhaus, W. Wurth, H. J. Elmers, and G. Schönhense, Nat. Mat. **16**, 615 (2017).
[43] C. Tusche, M. Ellguth, A. Krasyuk, A. Winkelmann, D. Kutnyakhov, P. Lushchyk, K. Medjanik, G. Schönhense, and J. Kirschner, Ultramic. **130**, 70 (2013).
[44] J. Braun, J. Minár, and H. Ebert, Phys. Rep. **740**, 1 (2018).
[45] J. Braun, Rep. Prog. Phys. **59**, 1267 (1996).
[46] S. Halilov, E. Tamura, D. Meinert, H. Gollisch, and R. Feder, J. Phys. Cond. Matt. **5**, 3859 (1993).
[47] S. Vosko, L. Wilk, and M. Nusair, Can. J. Phys. **58**, 1200 (1980).
[48] H. Ebert, *Electronic Structure and Physical Properties of Solids* (Springer, Berlin, 2000), p. 191.
[49] H. Ebert, D. Ködderitzsch, and J. Minár, Rep. Prog. Phys. **74**, 096501 (2011).
[50] H. Ebert *et al.*, The munich SPR-KKR package: [version 6.3 (http://olymp.cup.uni-muenchen.de/ak/ebert/SPRKKR)] (2012).
[51] G. Malmstrom and J. Rundgren, Comp. Phys. Commun. **19**, 263 (1980).
[52] A. Nuber, J. Braun, F. Forster, J. Minar, F. Reinert, and H. Ebert, Phys. Rev. B **83**, 165401 (2011).
[53] K. Medjanik, S. Babenkov, S. Chernov, D. Vasilyev, B. Schönhense, C. Schlueter, A. Gloskovskii, Y. Matveyev, W. Drube, H. Elmers, and G. Schönhense, J. Synchr. Rad. **26**, 1996 (2019).
[54] H. J. Elmers, D. Kutnyakhov, S. V. Chernov, K. Medjanik, O. Fedchenko, A. Zaporozhchenko-Zymakova, M. Ellguth, C. Tusche, J. Viefhaus, and G. Schönhense, J. Phys. Cond. Matt. **29**, 255001 (2017).
[55] V. N. Strocov, J. Electr. Spectr. Rel. Phenom. **229**, 100 (2018).
[56] M. Seah and W. Dench, Surf. Interface Analysis **1**, 2 (1979).
[57] J. Wiebe, F. Meier, K. Hashimoto, G. Bihlmayer, S. Blugel, P. Ferriani, S. Heinze, and R. Wiesendanger, Phys. Rev. B **72**, 193406 (2005).
[58] J. I. Pascual, G. Bihlmayer, Y. M. Koroteev, H.-P. Rust, G. Ceballos, M. Hansmann, K. Horn, E. V. Chulkov, S. Blügel, P. M. Echenique, and P. Hofmann, Phys. Rev. Lett. **93**, 196802 (2004).
[59] J. Wang, W. Li, P. Cheng, C. Song, T. Zhang, P. Deng, X. Chen, X. Ma, K. He, J.-F. Jia, Q.-K. Xue, and B.-F. Zhu, Phys. Rev. B **84**, 235447 (2011).
[60] L. El-Kareh, G. Bihlmayer, A. Buchter, H. Bentmann, S. Blügel, F. Reinert, and M. Bode, New J. Phys. **16**, 045017 (2014).
[61] K. Miyamoto, H. Wortelen, H. Mirhosseini, T. Okuda, A. Kimura, H. Iwasawa, K. Shimada, J. Henk, and M. Donath, Phys. Rev. B **93**, 161403(R) (2016).